






RESEARCH ARTICLE

Magnetic Resonance in Medicine

Accelerated B_1^+ mapping and robust parallel transmit pulse design for heart and prostate imaging at 7 T

Nico Egger¹  | Sophia Nagelstraßer¹ | Saskia Wildenberg^{1,2} | Andreas Bitz² | Laurent Ruck¹  | Jürgen Herrler³  | Christian Rainer Meixner³ | Ralph Kimmlingen³ | Titus Lanz⁴ | Sebastian Schmitter⁵  | Michael Uder¹ | Armin Michael Nagel^{1,6} 

¹Institute of Radiology, University Hospital Erlangen, Friedrich-Alexander-Universität Erlangen-Nürnberg (FAU), Erlangen, Germany

²Electrical Engineering and Information Technology, University of Applied Sciences – FH Aachen, Aachen, Germany

³Siemens Healthcare, Erlangen, Bavaria, Germany

⁴Rapid Biomedical, Rimpar, Germany

⁵Physikalisch-Technische Bundesanstalt (PTB), Braunschweig and Berlin, Germany

⁶Division of Medical Physics in Radiology, German Cancer Research Centre (DKFZ), Heidelberg, Germany

Correspondence

Nico Egger, Institute of Radiology, University Hospital Erlangen, Friedrich-Alexander-Universität Erlangen-Nürnberg (FAU), Maximiliansplatz 3, 91054 Erlangen, Bavaria, Germany.
Email: nico.egger@uk-erlangen.de

Abstract

Purpose: To investigate the impact of reduced k-space sampling on B_1^+ mapping and the resulting impact on phase shimming and dynamic/universal parallel transmit (pTx) RF pulse design.

Methods: Channel-wise 3D B_1^+ maps were measured at 7 T in 35 and 23 healthy subjects for the heart and prostate region, respectively. With these B_1^+ maps, universal phase shims optimizing homogeneity and B_1^+ efficiency were designed for heart and prostate imaging. In addition, universal 4kT-point pulses were designed for the heart. Subsequently, individual phase shims and individual 4kT-pulses were designed based on B_1^+ maps with different acceleration factors and tested on the original maps. The performance of the pulses was compared by evaluating their coefficients of variation (CoV), B_1^+ efficiencies and specific energy doses (SED). Furthermore, validation measurements were carried out for one heart and one prostate subject.

Results: For both organs, the universal phase shims showed significantly higher B_1^+ efficiencies and lower CoVs compared to the vendor provided default shim, but could still be improved with individual phase shims based on accelerated B_1^+ maps (acquisition time = 30 s). In the heart, the universal 4kT-pulse achieved significantly lower CoVs than tailored phase shims. Tailored 4kT-pulses based on accelerated B_1^+ maps resulted in even further reduced CoVs or a 2.5-fold reduction in SED at the same CoVs as the universal 4kT-pulse.

Conclusion: Accelerated B_1^+ maps can be used for the design of tailored pTx pulses for prostate and cardiac imaging at 7 T, which further improve homogeneity, B_1^+ efficiency, or SED compared to universal pulses.

KEYWORDS

7 tesla, B_1^+ mapping, heart, parallel transmission, prostate, ultra-high field

1 | INTRODUCTION

A key advantage of ultra-high field (UHF) MRI is the fact that the SNR grows superlinearly with increasing field strength,^{1,2} which especially benefits techniques with generally low sensitivity such as X-nuclei imaging³ or functional MRI.⁴ For ¹H imaging, potential advantages of UHF include achieving higher spatial resolutions, a reduction of measurement time or improved tissue contrast.⁵

However, increasing the main magnetic field strength also reduces the wavelength of the transmit RF field (B_1^+). For ¹H imaging at 7 T, the reduced wavelength can lead to an inhomogeneous B_1^+ field, resulting in spatially varying flip angles (FA) and, therefore, in non-optimal tissue contrast or local signal dropouts, especially for larger FOVs.⁶ To address this challenge, parallel transmit (pTx) methods have been developed, which make use of RF coils with multiple independent transmit channels.^{7–9} Paramount to the success of pTx methods is knowledge of the channel-wise transmit sensitivities, which are strongly dependent on the individual subject and RF coil positioning. For measuring these transmit sensitivities, a multitude of different B_1^+ mapping techniques exist.¹⁰ However, for cardiac and prostate imaging at UHF, several challenges such as high local specific absorption rates (SAR), a large FOV, the large dynamic range of the transmit field,^{11,12} increased B_0 off-resonances and motion from heartbeat and breathing¹³ hinder the applicability of most of these methods and result in long acquisition times for channel-wise B_1^+ maps. In addition, the need for organ-specific regions of interest (ROI) and online pTx pulse optimization further increases the preparation time.

One approach that eliminates these issues is the concept of universal pulses, which was originally introduced for brain applications¹⁴ and has recently been demonstrated to be feasible for cardiac imaging at 7 T.¹⁵ However, universal pulses optimized for FA homogeneity generally result in a lower uniformity at the same RF power or SAR level, compared to pulses that are tailored individually for each subject.^{14,15}

The aim of this work was to investigate whether tailored pTx pulses for body imaging could be achieved within tolerable calibration times by accelerating the B_1^+ mapping. The acceleration was done through undersampling, which was not mitigated other than by an additional Gaussian filter applied to the data. Since the aforementioned universal approaches represent a solution that does not require additional calibration time, we first designed universal pulses for prostate and cardiac imaging, which were then used as a benchmark to compare tailored pulses optimized on accelerated B_1^+ maps to. For this purpose, we measured relative channel-wise 3D B_1^+ maps of 35 heart and 23 prostate subjects and designed tailored phase

shims based on undersampled B_1^+ maps with different acceleration factors (ACFs) and universal phase shims for both organs. To evaluate their performance, the coefficients of variation (CoV) and the B_1^+ efficiencies of the phase shims were determined. For the heart, we also investigated tailored kT-point pulses optimized on accelerated B_1^+ maps and universal kT-point pulses, which were compared by their CoVs and specific energy doses (SED) (absorbed energy per tissue mass). The proposed methods were tested in vivo on one prostate and one heart subject outside the training data set.

2 | METHODS

2.1 | B_1^+ mapping methods

For the acquisition of relative channel-wise 3D B_1^+ maps, a method consisting of a series of gradient echo (GRE) images¹⁶ was used. During each acquisition only one of the N_{Tx} transmit channels is used for excitation, whereas the signal is measured with all of the N_{Rx} receive channels simultaneously. In the small FA regime, the channel-wise B_1^+ magnitude is related to the measured complex signal intensities $I_{n,m}(\mathbf{r})$ of transmit channel n and receive channel m via¹⁶:

$$|B_{1,n}^+(\mathbf{r})| = \frac{\sum_m^{N_{Rx}} |I_{n,m}(\mathbf{r})|}{\sqrt{c\rho_0(\mathbf{r}) \sum_m^{N_{Rx}} \sum_n^{N_{Tx}} |I_{n,m}(\mathbf{r})|}}. \quad (1)$$

Here, $\rho_0(\mathbf{r})$ refers to the proton density at position \mathbf{r} and c describes a spatially invariant scaling factor relating the B_1^+ field to the measured signal intensity. For this formula, it is assumed that the sum of magnitudes (SoM) of the receive fields B_1^- is equal to that of the transmit fields:

$$\sum_m^{N_{Rx}} |B_{1,m}^-(\mathbf{r})| = \sum_n^{N_{Tx}} |B_{1,n}^+(\mathbf{r})|. \quad (2)$$

For the RF coil used in this work, an evaluation of this assumption is shown in Figure S1. For the estimation of the relative transmit magnitudes $|\hat{B}_{1,n}^+(\mathbf{r})|$, the proton density and scaling factor in Eq. (1) are set to one, resulting in:

$$|\hat{B}_{1,n}^+(\mathbf{r})| = \frac{\sum_m^{N_{Rx}} |I_{n,m}(\mathbf{r})|}{\sqrt{\sum_m^{N_{Rx}} \sum_n^{N_{Tx}} |I_{n,m}(\mathbf{r})|}}. \quad (3)$$

Note that while the spatially invariant scaling factor has no effect on the relative B_1^+ magnitudes, neglecting the proton density leads to a bias in the maps that is proportional to the square root of $\rho_0(\mathbf{r})$.

The relative phases $\hat{\phi}_n(\mathbf{r})$ of each transmit channel (compared to a reference channel n_{ref}) are calculated from the measured signal intensities with¹⁷:

$$\hat{\phi}_n(\mathbf{r}) = \text{angle} \left[\sum_m^{N_{\text{Rx}}} I_{n,m}(\mathbf{r}) \cdot I_{n_{\text{ref}},m}^*(\mathbf{r}) \right]. \quad (4)$$

For robustness against motion,¹⁷ this relative B_1^+ mapping approach was implemented with a density-adapted 3D radial (DA-3D-rad) readout,^{18,19} acquiring full projections. Sequence parameters for the GRE acquisitions were: TR/TE = 4.5/2.02 ms, nominal FA = 8°, reference voltage = 280 V (based on pilot data), FOV = (320 mm)³, nominal resolution = (4 mm)³, readout duration = 2.5 ms, projections = 10 000, acquisition time (TA) = 6 min. A retrospective data reconstruction with different numbers of projections was enabled by a golden angle acquisition scheme.²⁰

For mapping absolute B_1^+ values, the actual flip angle imaging (AFI) method²¹ was used. The AFI sequence was implemented with a DA-3D-rad readout and acquired with a phase shim optimized for B_1^+ efficiency. Measurement parameters were: TR1/TR2 = 15/75 ms, TE = 3.03 ms, nominal FA = 70°, reference voltage = 600 V (based on pilot data), FOV = (320 mm)³, readout duration = 2.5 ms, nominal resolution = (4 mm)³, randomized x-y-spoiling,²² projections = 7500, TA = 11:15 min.

2.2 | Data acquisition

All measurements were carried out on a 7 T whole-body MR-system (MAGNETOM Terra, Siemens Healthcare) using an 8Tx/16Rx transceiver array (RAPID Biomedical). The array consists of an anterior and posterior part, each containing eight RF coil loops. For both parts these loops are arranged in a flower shape with one central and seven surrounding loops. In the transmit mode, two of the loops are combined with fixed amplitude and phase to one transmit channel (see Figure S2). To ensure a safe operation in pTx mode, the local and global SAR limits are met by limiting the time-averaged RF power of each transmit element to 1.195 W in first level mode.²³ Conformity to the IEC60601-2-33 was confirmed with a Declaration of Safety and Compatibility provided by the RF coil manufacturer. Before the examinations, each subject provided informed consent and all measurements were approved by the local ethics committee.

Care was taken to position the RF coil in a similar way for all subjects. For measurements of the heart, the edge of the RF coil was placed ~5 cm below the subject's chin. For measurements of the prostate, the edge of the array was placed near the subject's navel. The positioning laser was

used to align the RF coil in the isocenter. For the measurement of the B_1^+ maps, the acquisition FOV was not moved so that all maps were acquired at the isocenter. Acquisitions were carried out during free breathing with the subjects positioned in head-first direction for measurements of the heart and feet-first direction for the prostate.

In total, relative channel-wise B_1^+ maps were acquired from 35 healthy subjects (12 female, 23 male), yielding 35 maps of the heart and 23 maps of the prostate. For the total subject cohort, the age and body mass index (BMI) varied between 22 to 62 years (mean \pm SD = 28.1 \pm 8.2 years) and 16.4 to 32.2 kg/m² (22.8 \pm 3.2 kg/m²), respectively. For the group containing only the prostate (male) subjects, the age varied between 22 and 62 years (28.0 \pm 7.9 years) and the BMI between 16.4 and 32.2 kg/m² (23.4 \pm 3.2 kg/m²).

2.3 | Data processing

The measured data were reconstructed offline with a fast non-uniform Fourier Transform based gridding algorithm using the Berkeley Advanced Reconstruction Toolbox (BART).²⁴ The reconstructions of the GRE measurements were carried out for the initial number of measured projections (ACF 1, $N_{\text{Proj}} = 10\,000$) and for different acceleration factors (ACF 2–20 in steps of 2). Here, only the first $N_{\text{Proj}}/\text{ACF}$ projections were used for the reconstruction, which corresponds to a measurement with reduced scan time. In addition to a standard Hamming filter applied to the radial data, the raw data for the accelerated B_1^+ maps were Gaussian filtered. The Gaussian filter was implemented in the form of:

$$G(k) = e^{-2\pi^2 k^2 \tilde{\sigma}^2}. \quad (5)$$

Hereby, k describes the distance of the sampling point to the k -space center and $\tilde{\sigma}$ was set to 3 mm (see Figure S3). The resulting GRE images were then used to calculate the relative B_1^+ maps for each subject and ACF.

A default Volume Segmenter application in MATLAB (R2020b, The MathWorks) was used to define heart and prostate ROIs on the SoM images of the original B_1^+ maps. These ROIs were used as masks for the static and dynamic pulse design. Mean mask sizes were 565 \pm 115 cm³ for heart and 19 \pm 5 cm³ for prostate data. The relative B_1^+ maps of each subject and ACF were normalized by the mean signal intensity of the SoM within the corresponding ROI.¹⁵ Heart/prostate positions were determined by calculating the centroid voxel position of each subject's mask. Since all B_1^+ maps were acquired at the isocenter, organ positions were relative to this fixed point, enabling the calculation of a mean heart/prostate position. Euclidean distances between individual organ positions and the

isocenter and between individual and mean organ positions were then determined voxelwise and converted to millimeters via the image resolution.

For the dynamic pTx pulse design examined for the heart, estimated absolute B_1^+ maps were calculated following the approach outlined in Dietrich et al.¹⁷ For one subject, a scaling factor between the FA map (converted to $\mu\text{T/V}$) of an AFI measurement and the corresponding normalized, relative B_1^+ map was determined. The scaling factor was subsequently applied to all 35 normalized, relative B_1^+ maps of the heart, yielding absolute B_1^+ estimations.

2.4 | Static pTx pulse design

For the static pTx pulse design, phase-only shims were optimized by minimizing the cost function²⁵:

$$\text{cost} = (1 - \lambda) \cdot \text{CoV}^2 + \lambda \cdot \eta^{-2}. \quad (6)$$

The optimization aims to minimize the CoV:

$$\text{CoV} = \frac{\text{std}\left(\left|\sum_n^{N_{\text{Tx}}} B_{1,n}^+ \cdot e^{i\varphi_n}\right|\right)}{\text{mean}\left(\left|\sum_n^{N_{\text{Tx}}} B_{1,n}^+ \cdot e^{i\varphi_n}\right|\right)}, \quad (7)$$

which expresses the heterogeneity of the resulting B_1^+ distribution within the ROI and to maximize the B_1^+ efficiency η :

$$\eta = \text{mean}\left(\frac{\left|\sum_n^{N_{\text{Tx}}} B_{1,n}^+ \cdot e^{i\varphi_n}\right|}{\sum_n^{N_{\text{Tx}}} |B_{1,n}^+|}\right), \quad (8)$$

serving as a measure of the constructive interference between the transmit channels. Note that “ B_1^+ efficiency” is shortened to “efficiency” in the following and other efficiencies are explicitly labeled as such. The optimization parameter φ_n describes the global phase that is applied to the n^{th} transmit channel. The regularization parameter λ controls the weighting between heterogeneity and efficiency and was set to 0.025 for the heart and 0.3 for the prostate (see Figure S4). Optimizations were performed with MATLAB’s *fmincon* routine, using an interior-point algorithm. To avoid local minima, the process was repeated 100 times with randomized starting phase vectors.

Similar to the approach in Berrington et al.,²⁶ universal phase shims were calculated for heart and prostate by concatenating the B_1^+ maps and ROIs of the 35/23 subjects and jointly performing the optimization. Additionally, tailored phase shims were calculated for each subject and ACF. To quantify their performance, all phase shims were applied to the original B_1^+ map of the corresponding subject and CoVs and efficiencies were calculated within the ROI.

Tailored and universal phase shims were also compared to a vendor provided default phase shim, intended for cardiac imaging. The CoVs and efficiencies of the phase shims were tested for significant differences with a Wilcoxon signed rank test, testing the null hypothesis that the differences between two groups come from a distribution with a median of 0. The significance level was initially chosen as 0.05 and adjusted based on the number of comparisons carried out with a group, following the Bonferroni method. Statistically significant results were marked with (*) and non-significant results with “n.s.”

2.5 | Dynamic pTx pulse design

In addition to the static phase-only shims, dynamic pulses using a non-selective kT-point trajectory²⁷ were investigated for the heart. Following the results of Aigner et al.,¹⁵ the kT-point pulses were designed with four rectangular subpulses with a fixed duration of 0.15 ms each. For the three intervening gradient blips the duration was set to 0.09 ms, resulting in a total pulse duration of 0.87 ms. The target FA for the 4kT-point pulses was set to 5°.

The RF pulse forms of each transmit channel and the locations of the kT-points were optimized by evaluating a full Bloch simulation and minimizing the cost function²⁸:

$$\min_{\mathbf{b}, \mathbf{g}_{x,y,z}} \left\| \left| \text{Bloch}(\mathbf{b}, \mathbf{g}_{x,y,z}) \right| - \mathbf{m}_t \right\|_2^2, \quad (9)$$

subject to

$$\text{SED}(\mathbf{b}) \leq \text{SED}_{\text{max}}$$

and

$$\text{slew}(\mathbf{g}_{x,y,z}) \leq \text{slew}_{\text{max}}.$$

The channel-wise complex RF waveforms \mathbf{b} and the gradient blips $\mathbf{g}_{x,y,z}$ are optimized by minimizing the deviation between Bloch-simulated $\left(\left| \text{Bloch}(\mathbf{b}, \mathbf{g}_{x,y,z}) \right| \right)$ and target (\mathbf{m}_t) transversal magnetization. The optimization of RF waveforms and gradient blips is done simultaneously by an interior-point method based algorithm.^{29,30} The algorithm includes constraints for the pulse SED and the gradient slew rate, which were set to 0.1256 J/kg and 200 T/(m*s), respectively. The SED limit was chosen based on the channel-wise power limit of 1.195 W and the RF duty cycle of the DA-3D-rad sequence used for the validation measurement of the 4kT-point pulses. Because of the relatively short total pulse duration, off-resonance effects were neglected during the pulse design.³¹

A universal 4kT-point pulse (UP35-4kT) was designed by concatenating the B_1^+ maps of the 35 heart subjects and jointly running the optimization. To avoid local minima,

the optimization was repeated 1000 times with random initial values for the voltages (0–50 V) and phases (0– 2π) of each transmit channel and subpulse. The initial values for the gradient blips were set to zero. The $i = 1$ to 1000 calculated pulses were evaluated on the B_1^+ maps of each of the $j = 1$ to 35 subjects and the pulse with the minimum median CoV:

$$\text{CoV}_{opt} = \min_{i=1, \dots, 1000} \left(\text{median}_{j=1, \dots, 35} (\text{CoV}_{i,j}) \right), \quad (10)$$

of the resulting FA predictions was chosen as the best result. Subsequently, tailored-4kT pulses were designed for each subject and ACF. To achieve a robust and fast computation, the RF pulse and gradient shapes of UP35-4kT were used as initial values.³² Statistical analysis was performed as described in the static pTx pulse design section.

2.6 | Validation measurements

pTx pulses were tested on one prostate (male, 23 years, BMI = 24.7 kg/m²) and one heart subject (female, 22 years, BMI = 24.0 kg/m²) outside the training data set.

For the prostate measurements, 2D GRE and turbo spin echo (TSE) images were acquired with the default phase shim, UPS23, and tailored phase shims calculated on the original and 12-times accelerated B_1^+ maps. Sequence parameters for the GRE acquisitions

were: TR/TE = 200/3.57 ms, nominal FA = 17°, reference voltage = 800 V, FOV = 300 × 270 mm², resolution = 0.8 × 0.8 × 5.0 mm³, 22 slices, bandwidth = 400 Hz/Px, TA = 35 sec. Sequence parameters for the TSE acquisitions were: TR/TE = 15 730/134 ms, nominal FA = 116°, reference voltage = 800 V, FOV = 180 × 190 mm², resolution = 0.3 × 0.3 × 3.0 mm³, 5 slices, GRAPPA (PE: 2), deep resolve, turbo factor = 35, echo spacing = 8.36 ms, bandwidth = 406 Hz/Px, TA = 5:17 min.

For the heart, DA-3D-rad images were acquired with the default phase shim, UP35-4kT, and tailored-4kT pulses calculated on the original and 12-times accelerated B_1^+ maps. Sequence parameters were: TR/TE = 7.1/2.02 ms, nominal FA = 5°, reference voltage = 800 V (default phase shim), FOV = (320 mm)³, nominal resolution = (1.4 mm)³, readout duration = 2 ms, half projections, projections = 60 000, TA = 7:06 min.

3 | RESULTS

3.1 | Distribution of tailored and universal phase shims

Figure 1 depicts the channel-wise phases of the tailored, universal and default phase shims for heart (Figure 1A) and prostate (Figure 1B). The phases of the tailored shims show a similar distribution over the different subjects. The

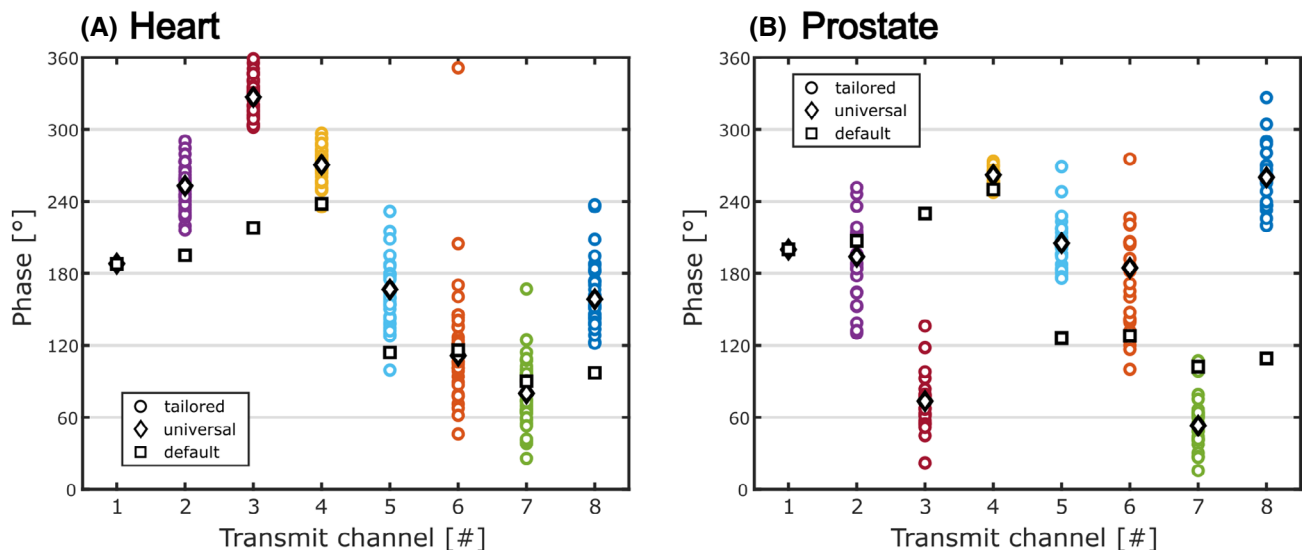


FIGURE 1 Channel-wise phases of the default phase shim, the tailored shims, and the universal shim optimized for heart (A) and prostate (B). The tailored shim phases of the 35/23 subjects are represented as circles and are divided into colors according to the corresponding transmit channel. The universal shim phases are indicated as black diamonds and the default shim phases as black squares. For a better comparison, shim phases were calculated relative to the phase of the first channel, which was set to 0°. To (mostly) avoid phase wraps, an arbitrary constant phase offset was added to all values. For both organs and between the different subjects, the tailored shim phases of each channel show a tendency to cluster around a common phase, although outliers can be observed for some of the channels. In general, the universal shim phases appear to be close to the center of the clustered tailored phases. Averaged over all transmit channels, the difference between universal shim phases and mean of the tailored shim phases (not depicted) is less than 3° for both organs.

mean channel-wise variation of the tailored shim phases (difference between maximum and minimum phase, averaged over all transmit channels) is $99^\circ \pm 65^\circ$ for the heart and $91^\circ \pm 55^\circ$ for the prostate. The universal shim phases match the distribution of the tailored shim phases. The difference between the universal shim phases and the mean of the tailored shim phases averaged over all transmit channels is $1.8^\circ \pm 1.6^\circ$ (heart) and $2.2^\circ \pm 3.2^\circ$ (prostate). In comparison, for the default phase shim, this difference has a mean value of $41^\circ \pm 37^\circ$ for the heart, and $64^\circ \pm 61^\circ$ for the prostate.

3.2 | Performance of tailored and universal phase shims

Figure 2 shows the homogeneity and efficiency of universal and tailored phase shims compared to the default

phase shim applied to all heart/prostate subjects. In the heart (Figure 2A), the default shim yields a median CoV of 29.1% and no value under 20%. UPS35 achieves a reduction of the median CoV to 18.7% and a smaller variation between the subjects (range = 15.9%–29.0%). For the tailored phase shims the CoVs are reduced further to a median value of 17.3% (range = 14.9%–23.7%). For UPS35 three outliers can be observed, two of which are also present for the tailored phase shims and correspond to the two subjects with the largest heart volumes. Regarding the efficiencies (Figure 2B), the default phase shim achieves a median of 53.7%, which increases to 63.3% for UPS35 (range = 58.2%–67.5%). Compared to the universal shim, the tailored phase shims show only minor increases to a median efficiency of 64.0% with comparable variations.

For the prostate region (Figure 2C), the default phase shim yields a lower median CoV compared to the heart

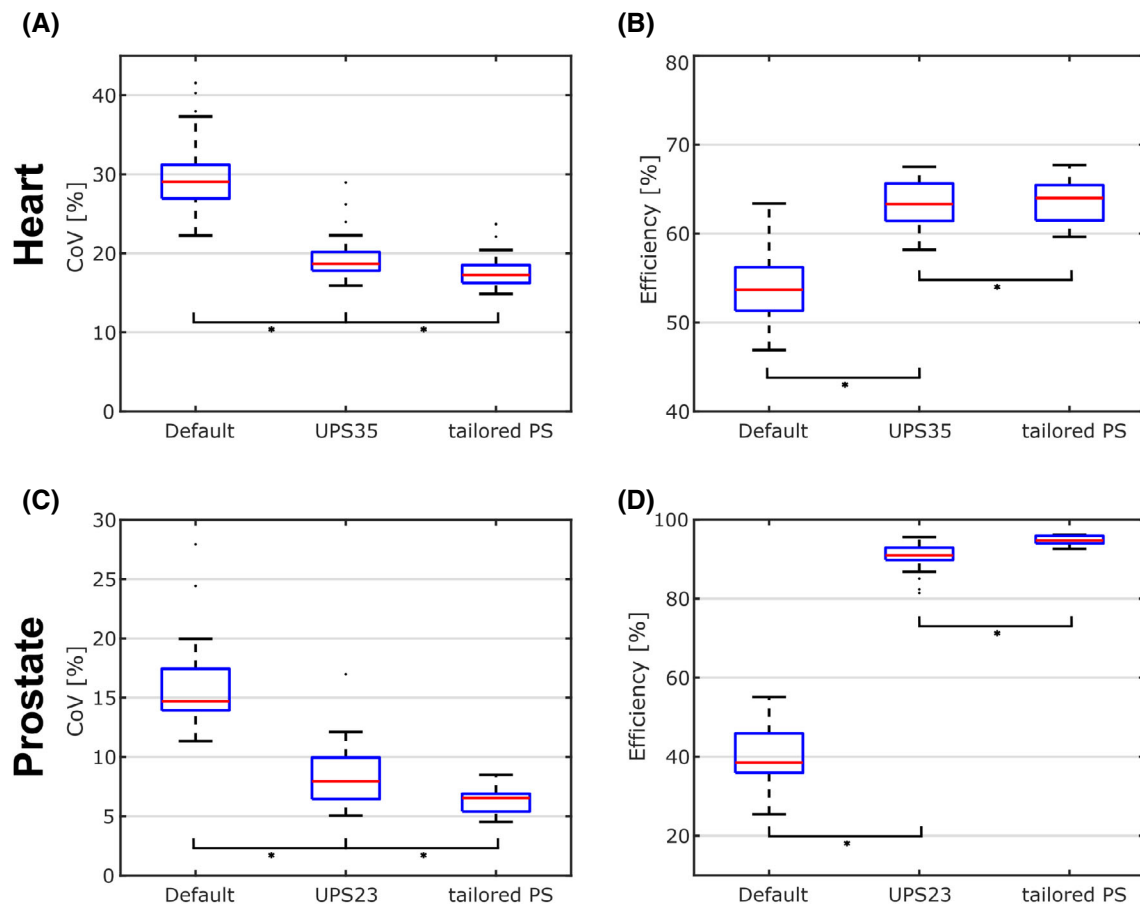


FIGURE 2 Performance of the universal phase shims for heart (UPS35, see A,B) and prostate (UPS23, see C,D) compared to the vendor provided default phase shim and the subject specific tailored phase shims (tailored PS). The boxplots depict the coefficients of variation (CoVs) (A,C) and efficiencies (B,D) calculated from the predicted B_1^+ distributions that result from applying the corresponding phase shim to the B_1^+ maps of each of the 35/23 subjects. Over all subjects the universal phase shims achieve lower median CoVs and higher median efficiencies in both organs compared to the default phase shim. Comparing the universal phase shims to the tailored PS, the tailored shims show a further reduction in the median CoVs and increase in median efficiencies. The improvements from universal to tailored PS are smaller than from default to universal phase shims, but the differences are statistically significant in all cases, as denoted by the asterisk (*).

of 14.7%, which can be explained by the smaller ROI. For UPS23 a reduction of the median CoV to 7.9% with a 75th percentile of under 10% is achieved. The tailored phase shims further reduce the median CoV to 6.5% and result in a smaller variation. For the efficiency (Figure 2D), applying the default phase shim leads to a low median value of 38.5% and a large variation over all 23 subjects (range = 25.4%–55.1%). UPS23 shows an increase in the median efficiency to 90.9% with efficiencies above 80% for all subjects. A further increase to a median efficiency of 94.7% is observed for the tailored phase shims. Importantly, the range between the subjects is very small with

variations of the efficiencies between 92.6% and 96.1% and no outliers.

3.3 | Influence of subject positioning

In Figure 3 the homogeneities and efficiencies of the universal and tailored phase shims are displayed over the distance to the mean heart/prostate position. For the CoVs in the heart (Figure 3A), both the universal and the tailored phase shims show an increase with rising distance from the mean heart position. As the linear fit indicates,

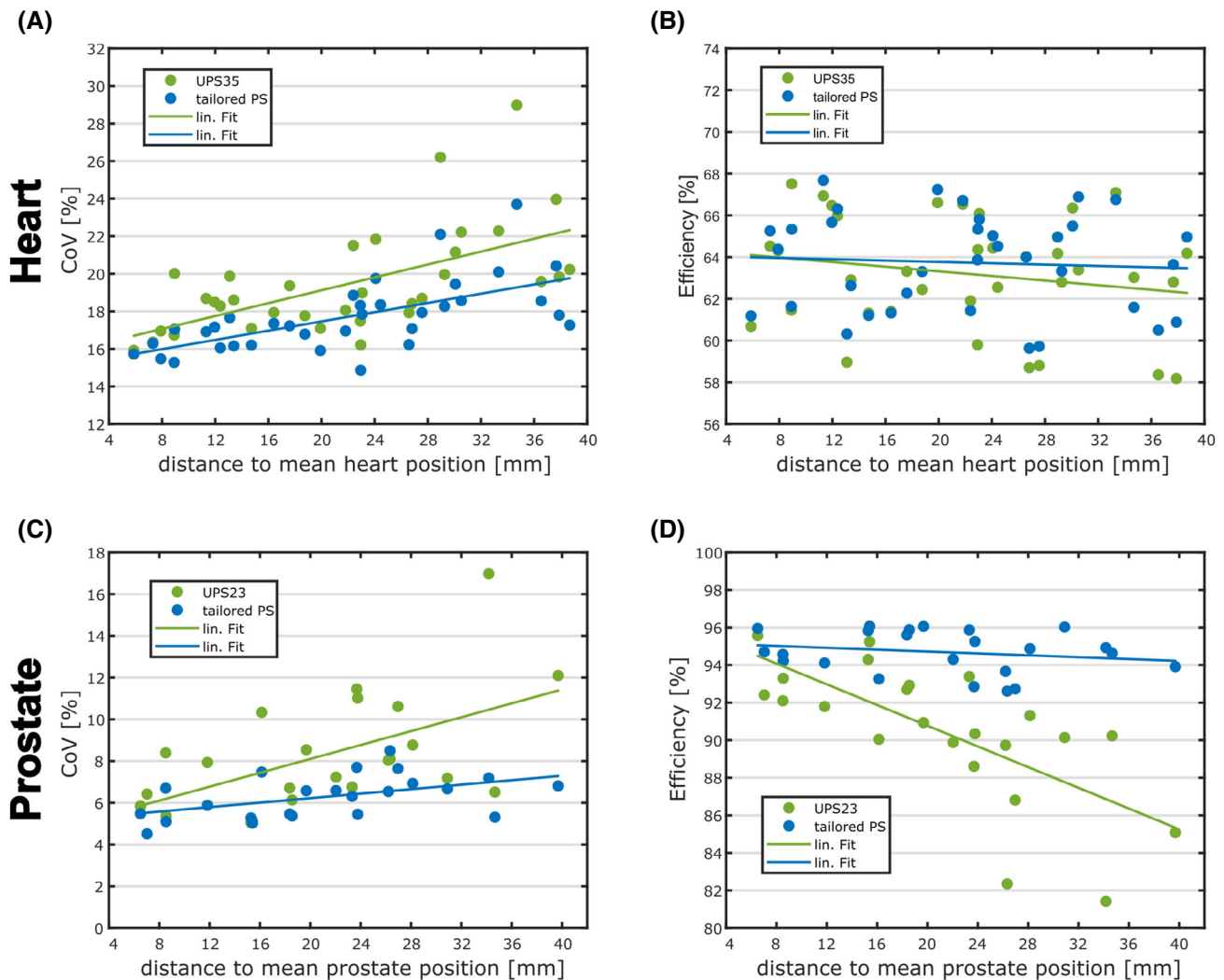


FIGURE 3 Influence of subject positioning on the performance of the universal phase shims for heart (UPS35, see A,B) and prostate (UPS23, see C,D) and the tailored phase shims (tailored PS). Individual organ positions were determined by calculating the centroid of the corresponding mask. The graphs depict the coefficients of variation (CoVs) (A,C) and efficiencies (B,D) resulting for each subject and shim set as a function of the distance to the mean heart/prostate position averaged over all subjects. For the prostate, the tailored PS show almost no or only a minor correlation with the mean prostate position, whereas both the CoVs and efficiencies of the universal phase shim clearly deteriorate with higher distance from the mean. For the efficiencies in the heart, a similar effect can be observed although the decrease of the universal shim is less severe than in the prostate. For the CoVs, both the tailored and the universal shims show an increase with higher distance to the mean heart position with a slightly higher rate for the universal shim.

the rate of increase is higher for the universal shim. For the efficiency (Figure 3B), the tailored phase shims show almost no correlation with the distance whereas for UPS35 a slight decrease with increasing distance can be observed.

For the prostate, a notable increase in CoV (Figure 3C) and decrease in efficiency (Figure 3D) with increasing distance from the mean position can be seen for UPS23. The CoVs and the efficiencies of the tailored phase shims show only a minor correlation with the distance of the mean prostate position.

For both organs, the correlation between the distance to the mean position and the distance to the isocenter is shown in Figure S5.

3.4 | Influence of acceleration on the relative B_1^+ maps

Figure 4 depicts the relative B_1^+ magnitude and phase maps reconstructed from data with different ACFs for one heart subject (Figure 4A) and one prostate subject (Figure 4B). The maps are shown exemplary for one anterior and one posterior transmit channel (all channels are shown in Figure S6). Qualitatively, the pattern of the B_1^+ magnitude in both organs shows a good agreement between the different accelerations. Nevertheless, the lower SNR resulting from fewer projections and incoherent undersampling artifacts are visible, especially in areas with low

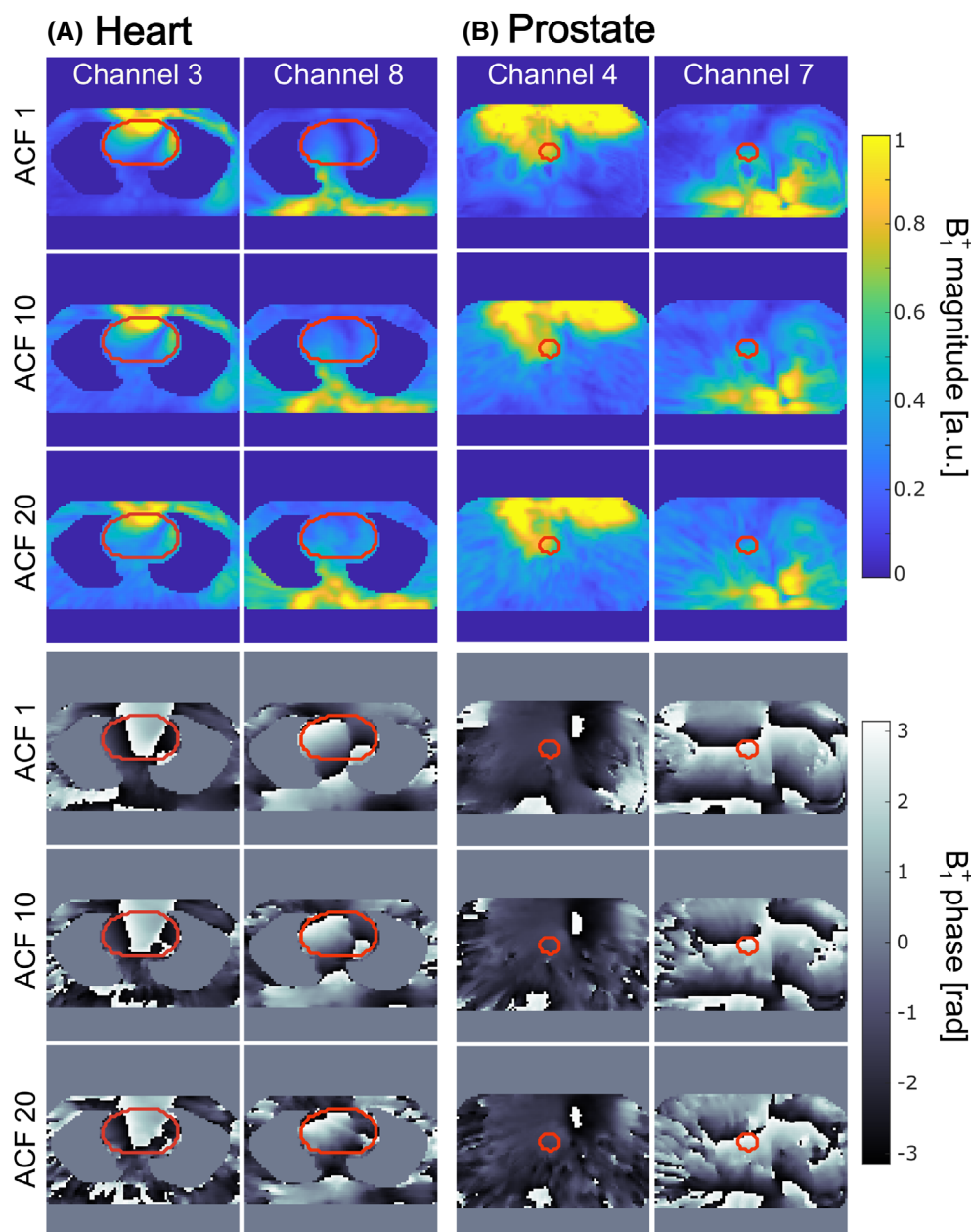


FIGURE 4 Comparison of the relative B_1^+ magnitude and phase maps of one heart subject (A) and one prostate subject (B) obtained for acceleration factor (ACF) 1, 10, and 20. For both organs one channel of the posterior and one channel of the anterior part of the RF coil array are shown (a full channel-wise overview is given in Figure S6). The contours of the 2D masks corresponding to the illustrated slices are outlined in red. The lower SNR and noise-like undersampling artifacts resulting from the reduced number of measured projections are visible in the accelerated B_1^+ maps and increase with higher ACFs. Nevertheless, the general pattern of the B_1^+ magnitude and phase is still preserved even for high ACFs.

magnitude. In these areas, some of the B_1^+ information might be lost at higher ACFs, as can be seen in the signal void within the heart for transmit channel 8. A similar effect can also be observed for the phase data. An evaluation of the direct differences between the original and accelerated B_1^+ maps is included in Figures S7 and S8.

3.5 | Influence of acceleration on tailored phase shims

A quantitative comparison of the CoVs and efficiencies of tailored phase shims optimized on B_1^+ maps with different ACFs is shown in Figure 5. For the CoV in the heart (Figure 5A), increasing the ACF results in a higher median value, increasing from 17.3% to 18.2% between ACF 1 and ACF 20. For the efficiency (Figure 5B) no clear trend can be

observed. In both cases, the variation of CoVs and efficiencies increases until ACF 20 from 8.8% to 10.8% for the CoV and from 8.1% to 12.6% for the efficiency. For a pre-defined goal of reaching a tolerable B_1^+ mapping time of 30 s (\triangleq ACF 12), a median CoV of 17.6% and median efficiency of 64.1% is achieved. For the CoV, the differences between UPS35 and the tailored phase shims are significant up to ACF 18, whereas for the efficiency the differences are not significant.

Similar to the efficiencies in the heart, the median CoVs in the prostate (Figure 5C) show no clear trend for increasing ACFs. The efficiencies (Figure 5D) slightly decrease from a median value of 94.7% to 93.9% between ACF 1 and 20. Additionally, the range of efficiencies between the 23 subjects increases from 3.5% to 6.0% at ACF 20. The tailored phase shims with ACF 12 yield a median CoV of 6.3% and a median efficiency of 94.2%. For both the

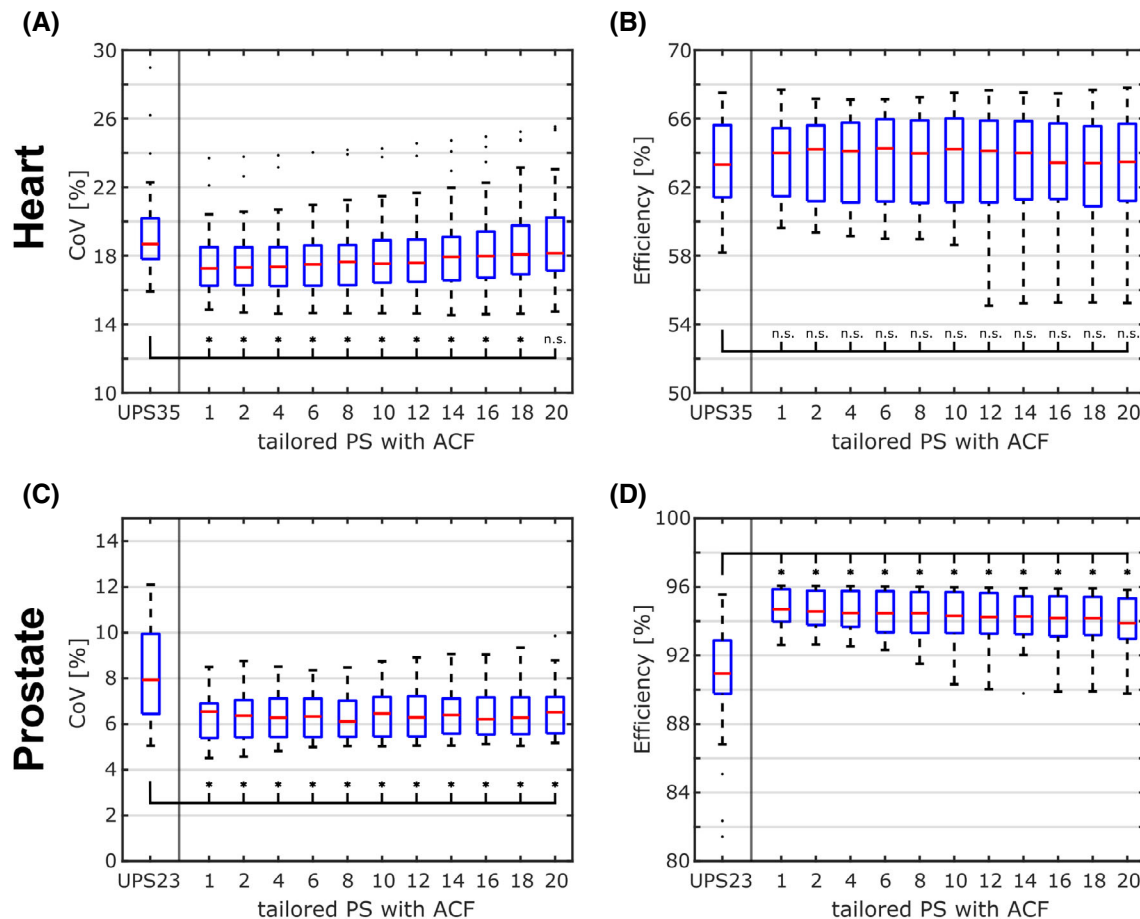


FIGURE 5 Performance of tailored phase shims (tailored PS) optimized on B_1^+ maps with varying acceleration factors (ACFs) for heart (A,B) and prostate (C,D). The boxplots show the coefficients of variation (CoVs) and efficiencies over all 35/23 subjects and for a comparison also include the respective universal phase shims (UPS35/UPS23). For the CoV in the heart (A) and the efficiency in the prostate (D), an increasing ACF leads to both a deterioration of the median value as well as a higher variance between the individual subjects. For the efficiency in the heart (B) and the CoV in the prostate (C), the median values show no clear trend for increasing ACFs, but rather a fluctuation around the values obtained with ACF 1. Statistical analysis was performed to compare the results of the tailored shims with the results of the universal phase shims. Significant differences are marked with (*) and non-significant differences are denoted with "n.s."

CoV and the efficiency, the differences between UPS23 and the tailored phase shims are significant for all ACFs.

Figure 6 depicts predicted B_1^+ magnitude and efficiency maps for a representative heart (Figure 6A) and prostate subject (Figure 6B). Compared to the default phase shim, which generally shows the worst performance, the universal phase shims achieve improved homogeneity and increased efficiency in both organs. A further improvement can be observed for the tailored phase shims with ACF 1. For the tailored phase shims with a B_1^+ mapping

time of 30 s (ACF 12) the results are similar to the shims with ACF 1 with small increases of 17.2% to 17.7% for the CoV and 62.3% to 62.7% for the efficiency.

3.6 | Performance of universal and tailored 4kT-point pulses in the heart

In addition to the phase shims, universal and tailored 4kT-point dynamic pTx pulses optimized on B_1^+ maps with

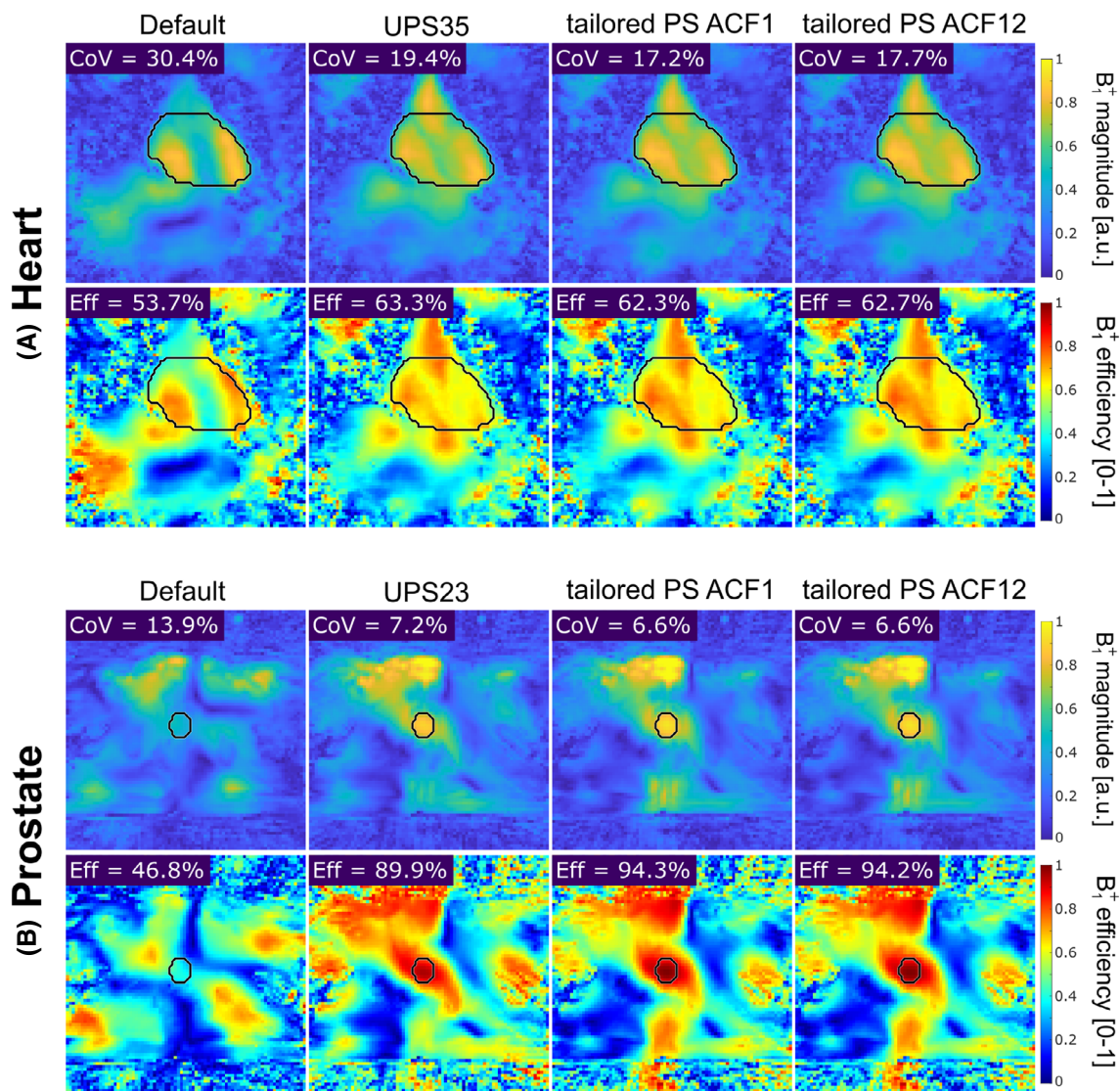


FIGURE 6 Predicted B_1^+ magnitude and efficiency maps for heart subject 26 (A) and prostate subject 15 (B) resulting from the default phase shim, the corresponding universal phase shim (UPS35/UPS23), the tailored phase shim optimized on the original B_1^+ map (tailored PS ACF 1) and the tailored PS optimized on the B_1^+ map reconstructed with acceleration factor (ACF) 12 (tailored PS ACF 12). The predicted maps are shown for a coronal slice of the heart and a transversal slice of the prostate. The mask that was used for the optimization and for the quantification is outlined in black. The coefficients of variation (CoVs) and the efficiencies, which result from the corresponding phase shims, are specified in the upper left corner. Note that the values are calculated over the whole 3D mask volume of which only a 2D section is shown. Applying the universal phase shim improves CoV and efficiency in both organs. Tailored PS optimized on B_1^+ maps with ACF 1 and ACF 12 result in very similar values and show a further improved homogeneity and efficiency compared to the universal phase shim.

different ACFs were investigated for the heart. Figure 7A shows a comparison of the CoVs resulting from the tailored phase shims, UP35-4kT, and the tailored-4kT pulses calculated from the original B_1^+ maps. Compared to the tailored phase shims, UP35-4kT yields a lower median CoV of 10.6% over all subjects with values between 8.5% and 15.3%. A further reduction to a median CoV of 5.7% with smaller variations between 4.6% and 7.6% is achieved with the tailored-4kT pulses.

Figure 7B shows the CoVs of tailored-4kT pulses optimized on B_1^+ maps with different ACFs. With rising ACF, a steady increase in the median CoV and inter-subject variations is observable, reaching a median value of 10.5% for ACF 20. Additionally, from ACF 2 onward a strong outlier value for subject 6 can be observed, which likely can be attributed to motion (see Figure S9). For a B_1^+ mapping time of 30 s (ACF 12), the tailored-4kT pulses result in a median CoV of 8.4% with a range of 5.7% to 12.2% (excluding the outlier at 18.9%). The differences between the CoVs of UP35-4kT and the tailored-4kT pulses are statistically significant up to ACF 16.

For a further approach, tailored-4kT pulses with ACF 1 and ACF 12 were designed, for which the SED constraints for the optimization were lowered gradually until an equal median CoV to UP35-4kT was reached. As can be seen in Figure 8A, all pulses result in a median CoV of 10.6% with comparable variations when applied to the 35 subjects. Figure 8B shows the mean SED of the pulses relative to the SED of UP35-4kT. Matching the median CoV of the universal pulse leads to a mean relative SED of $29.84\% \pm 0.02\%$

for the tailored-4kT pulses with ACF 1 and a mean relative SED of $40.54\% \pm 0.05\%$ for the tailored pulses with ACF 12.

3.7 | Experimental validation

In Figure 9, B_1^+ simulations of the homogeneity and efficiency, as well as GRE and TSE measurements are depicted for the default phase shim, UPS23 and tailored phase shims calculated on the original and 12-times accelerated B_1^+ maps for a prostate subject outside the training data set. For this subject, UPS23 yields a CoV of 5.9% and efficiency of 92.9%, which is comparable to the values achieved for subjects included in the training data. The improved efficiencies of the tailored and universal phase shims result in a highly improved image quality compared to the default shim and especially for the TSE acquisition, this enables the desired contrast in the prostate. Overall, the B_1^+ simulations and the GRE/TSE images of the prostate are in good agreement.

Figure 10 shows the FA predictions (Figure 10A) and the corresponding DA-3D-rad images (Figure 10B) for the default phase shim, UP35-4kT, and tailored-4kT pulses calculated on the original and 12-times accelerated B_1^+ maps for a heart subject outside the training data set. The tailored-4kT pulses were calculated using the more restrictive SED limits, resulting in the same median CoV for the 35 optimization subjects as UP35-4kT (see Figure 8). For the default shim, both the prediction and the measurement show areas with low FA and relatively large variations.

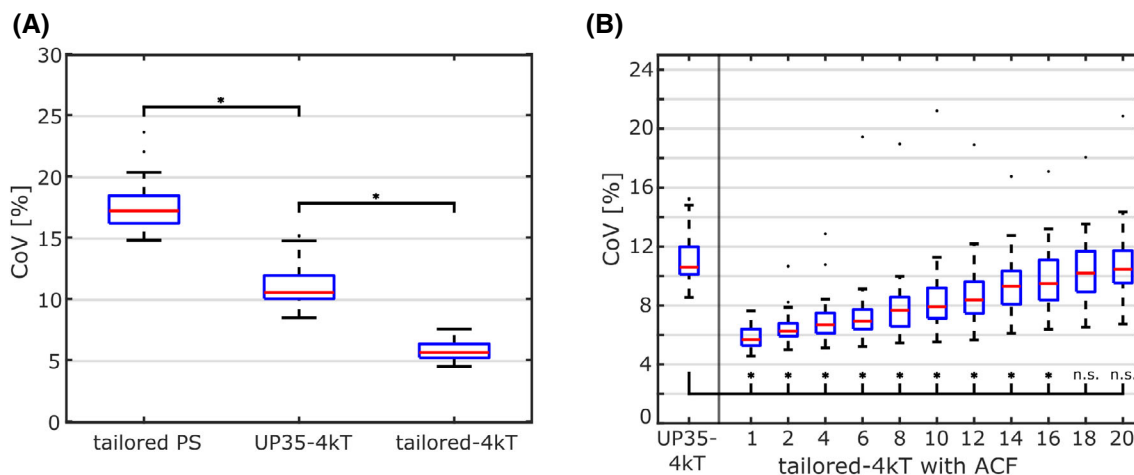


FIGURE 7 (A) Comparison of the coefficients of variation (CoVs) achieved in all 35 subjects in the region of the heart with tailored phase shims (tailored PS), UP35-4kT, and tailored-4kT pulses calculated on the original B_1^+ maps. The UP35-4kT results in improved homogeneity compared to the tailored PS, indicated by the reduced CoVs. Tailoring 4kT pulses individually for each subject achieves a further improvement of the homogeneity and a smaller range of CoVs. (B) CoVs of tailored-4kT pulses calculated for the 35 heart subjects on B_1^+ maps with varying acceleration factors (ACFs). The median CoVs as well as the variation between the subjects steadily increase with higher ACFs. For ACF 2 and higher, a strong outlier for subject 6 can be observed, which is attributed to subject motion (see Figure S9). Statistically significant differences to UP35-4kT are marked with (*) and non-significant differences are denoted with “n.s.”.

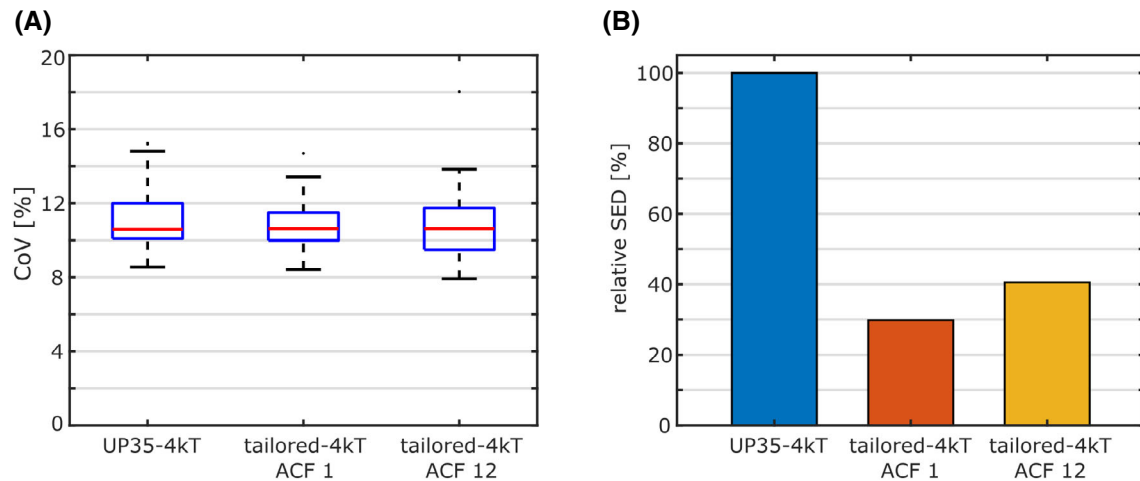


FIGURE 8 (A) Coefficients of variation (CoVs) of UP35-4kT compared to CoVs of tailored-4kT pulses with acceleration factor (ACF) 1 and 12 that were optimized with more restrictive specific energy dose (SED) constraints. For both ACFs, the SED limit was lowered separately until the median CoV of the corresponding tailored-4kT pulses matched the median CoV of 10.6% of UP35-4kT. (B) Mean SED values of the tailored-4kT pulses shown in (A) relative to the (single) SED value of UP35-4kT. With the goal of achieving a similar homogeneity as the universal pulse, the SED values of the tailored-4kT pulses with ACF 1 are reduced to ~30% and the SED values of the tailored-4kT pulses with ACF 12 to ~40% of the SED of UP35-4kT.

UP35-4kT achieves a CoV of 10.6% for this subject and the validation measurement shows a homogenous signal intensity throughout the heart. A comparable image quality is achieved with the tailored-4kT pulses, but at reduced SED levels. In general, there is a good match between simulated FA distributions and validation measurements.

4 | DISCUSSION

As part of this work, universal phase shims were designed for heart and prostate regions. Compared to the vendor provided shim intended for cardiac imaging, the universal phase shims showed a significant improvement in homogeneity and efficiency for both organs. The decent performance of universal phase shims can be explained with the similarity in phase distributions that was observed for individual phase shims. This also matches with previously reported results of calibration-free regional RF shims²⁶ optimized for small regions in the brain, although magnitude and phase shims were used in that case. Universal magnitude and phase shims have also been designed for the heart¹⁵ with comparable, but slightly worse homogeneity than the universal phase shim optimized in this work (median CoV of 25% vs. 17.8%), which might be explained by differences in the RF coil design or different optimization approaches. A disadvantage that remains for the universal phase shims is the observed dependence on subject positioning. Especially in the prostate, a clear deterioration in homogeneity and efficiency was seen for increasing distance from the mean organ position. The

stronger effect on UPS23 can be explained by the smaller organ size of the prostate, which results in a universal phase shim that is extremely local.

As expected, the homogeneity and efficiency of the phase shims is further improved by optimizing them individually for each subject, although this comes at the cost of additional calibration time. To shorten this process, we investigated the possibility of accelerating the B_1^+ mapping through undersampling. For the accelerated B_1^+ maps, qualitatively, a good agreement to the original maps was observed even for higher ACFs. A reason for this stability could be the fact that B_1^+ information has inherently low spatial frequency and the radial readout extensively samples the k-space center. The initial number of 10 000 projections was chosen to fulfill the Nyquist criterion assuming a spherical FOV and an isotropic resolution of 320 mm and 4 mm, respectively.³³ However, due to the low spatial frequency of the B_1^+ information and because of the fact that the single channel GRE measurements likely excite a FOV smaller than 320 mm, the original B_1^+ maps are presumably oversampled to a certain degree, which, however, is difficult to determine precisely. This also means that the acceleration factors are not directly equivalent to undersampling factors. Additionally, the Gaussian filter applied to the accelerated B_1^+ maps further reduces the effective resolution and helped in slightly lessening the effect of the undersampling. Instead of applying additional filters, another approach could be acquiring the data with lower initial resolution, which would reduce the number of projections needed to fulfill the Nyquist criterion. However, in a preliminary evaluation, this approach resulted

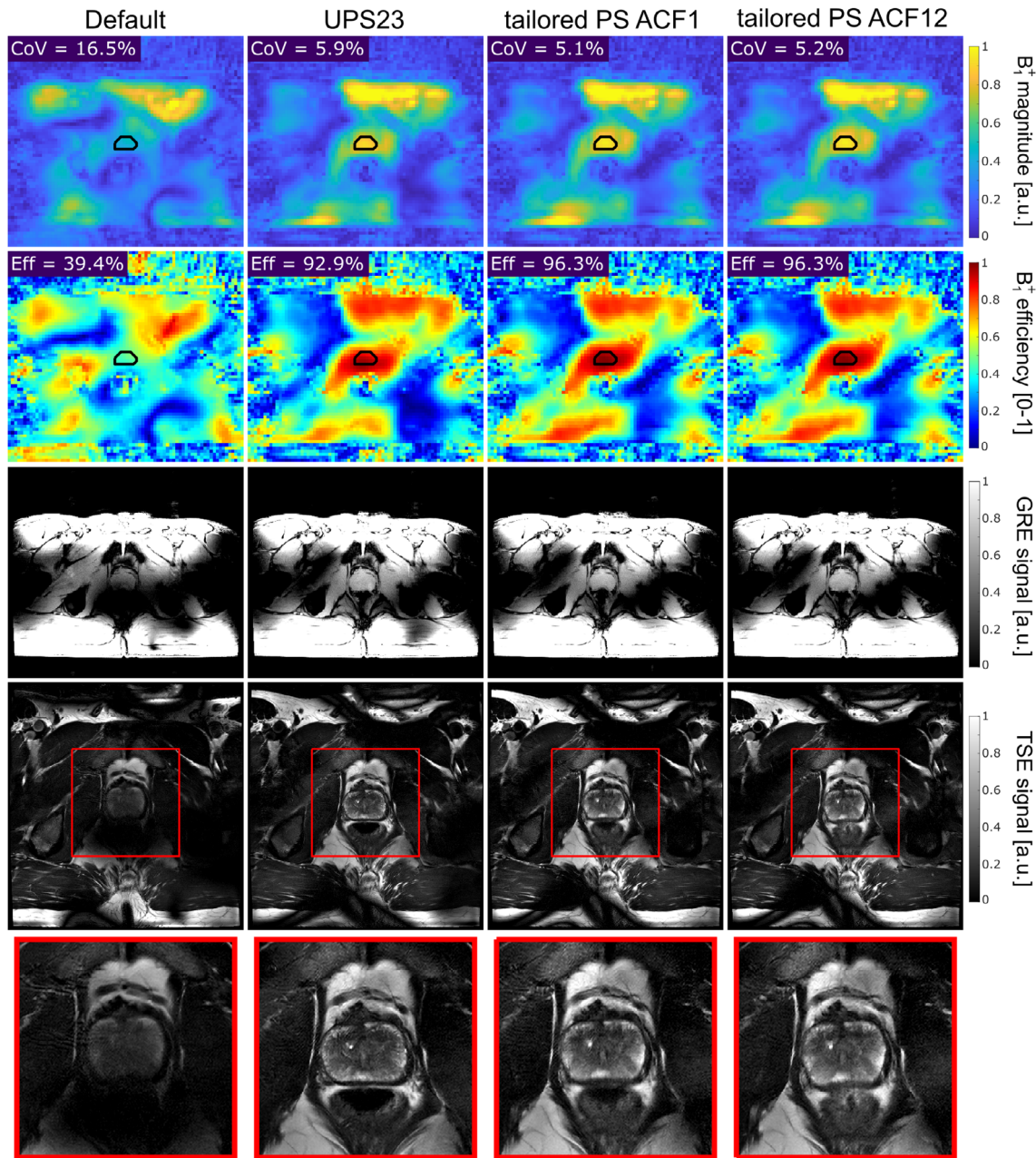


FIGURE 9 B_1^+ simulations of homogeneity and efficiency and validation gradient echo (GRE)/turbo spin echo (TSE) measurements for a prostate subject outside of the training data set. The measurements were acquired with the default phase shim, UPS23 and tailored phase shims calculated on the original and the 12-times accelerated (acquisition time = 30 s) B_1^+ maps. Compared to the default phase shim, the universal and tailored shims show a reduced coefficient of variation (CoV) and a considerably increased efficiency. The increased efficiency can also be seen in the improved image quality of the GRE and TSE acquisitions. Especially for the TSE acquisition, the default shim does not reach the required flip angle (FA) to achieve the intended contrast. The universal and tailored phase shims all result in a very similar image quality.

in a worse performance than acquiring the data at 4 mm resolution and applying the Hamming and Gaussian filters (see Figure S10). More importantly, quantitatively, the phase shims optimized on the accelerated B_1^+ maps showed only slight increases in CoVs (heart) and decreases in efficiencies (prostate) over all subjects. For a tolerable B_1^+ mapping time of 30 s, which is close to calibrations

times achieved in brain applications,^{32,34} the tailored phase shims still result in a significantly improved homogeneity/efficiency compared to the universal phase shims.

For the prostate, phase shims seem to be sufficient to achieve an acceptable homogeneity and high efficiencies, which agrees with the results of previous publications.³⁵ However, for larger ROIs, they are limited by their

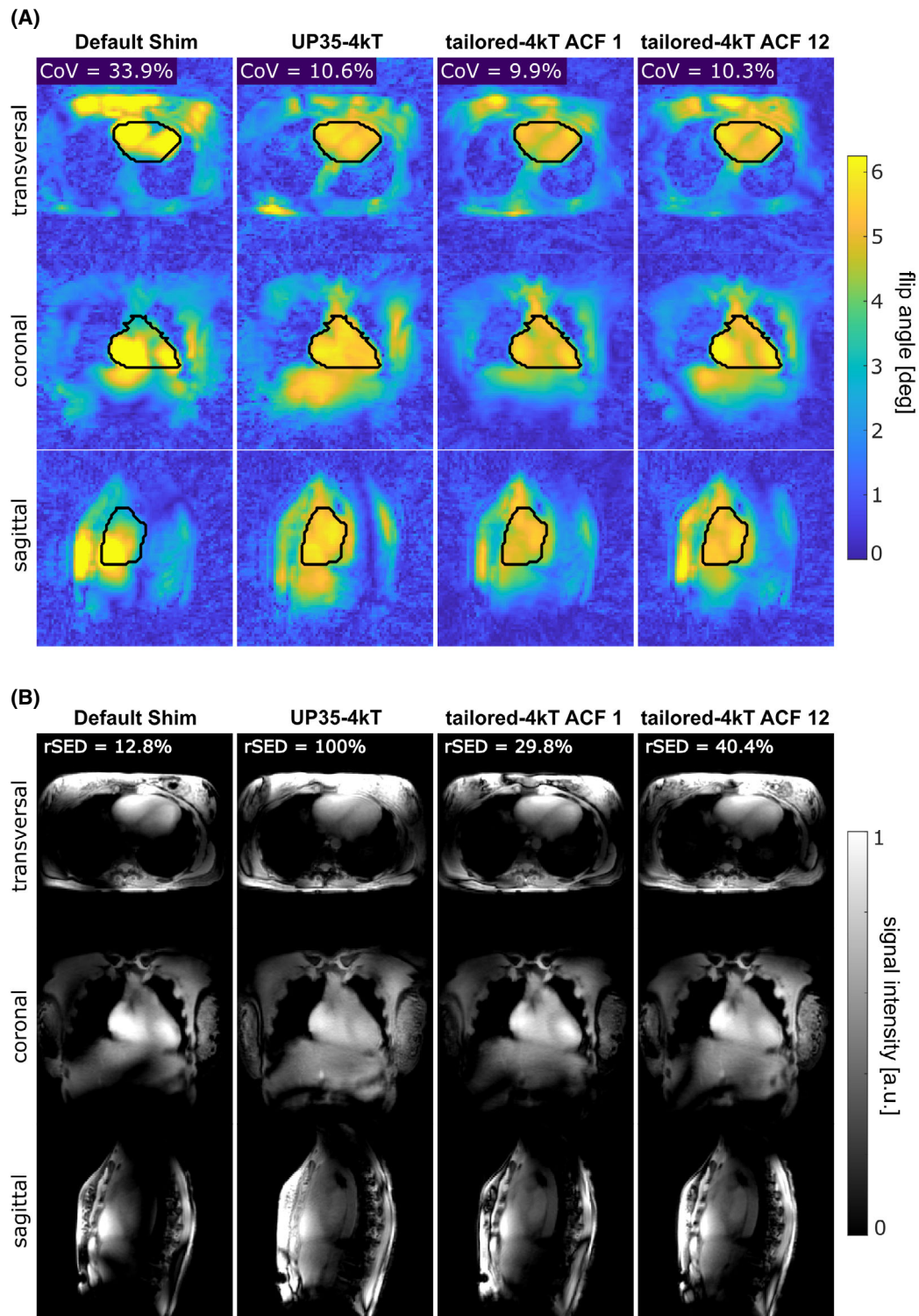


FIGURE 10 Flip angle (FA) predictions (A) and validation measurements with a density-adapted 3D radial (DA-3D-rad) sequence (B) for the default phase shim, UP35-4kT, and tailored-4kT pulses calculated on the original and the 12-times accelerated (acquisition time = 30 s) B_1^+ maps for a subject outside of the training data set. For the calculation of the tailored-4kT pulses, the more restrictive specific energy dose (SED) limits were used, which led to an equal median coefficient of variation (CoV) over the 35 optimization subjects as UP35-4kT (see Figure 8). For the simulation of the default phase shim, the FAs were scaled to reach a mean value of 5° . The CoV values resulting from the FA predictions and the SED values of the pulses relative to the SED of UP35-4kT are given at the top. Note that the SED value for the default shim is not directly comparable, as with the chosen reference voltage of 800 V, the mean FA likely differs from that of the dynamic pulses. The 4kT-point pulses all exhibit a similarly good image quality and improved homogeneity compared to the default phase shim. For the tailored-4kT pulses, a comparable level of homogeneity is reached at reduced SED values. Qualitatively, there is a good agreement between the FA predictions and the validation measurements.

restricted degrees of freedom³⁶ leading to higher CoVs and lower efficiencies in the heart. This could also be seen by the outliers for the CoVs of the tailored and universal phase shims, which corresponded to the two subjects with the largest heart volumes. For a full coverage of the heart and larger organs in general, more sophisticated pulses are needed.^{15,37,38} In line with these observations, dynamic 4kT-point pulses achieved a significantly improved homogeneity in the heart compared to tailored phase shims. For the universal kT-pulse, the results of Aigner et al.¹⁵ could be reproduced. Even with our different RF coil, optimization processes and constraints, similar homogeneity was observed (median CoV of 12.8% vs. 10.6%). However, since our universal pulses were evaluated on subjects included in the training set, their performance is exaggerated. An estimate of the extent of this exaggeration is shown in Figure S11 and indicates a rather small effect.

As expected due to the higher complexity, the acceleration had a bigger impact on the 4kT-point pulses than on the phase shims. Nevertheless, for a B_1^+ mapping time of 30 s, tailored pulses still resulted in a significant improvement in homogeneity compared to UP35-4kT. However, since the universal pulse already achieves acceptable homogeneity, a more important aim for tailored pulses might be the reduction of SED. Here, tailored-4kT pulses based on B_1^+ maps acquired in 30 s, resulted in a 2.5-fold SED reduction compared to UP35-4kT, while maintaining comparable CoVs. Reducing SED is of particular importance, as several cardiac imaging sequences benefit from high FA RF pulses.

One limitation of our study is that the relative B_1^+ maps are affected by errors introduced due to the assumptions made for their calculation. The assumption that the SoM of the receive fields is equal to that of the transmit fields is not completely correct. As shown in Figure S1 for the electromagnetic field simulations of the Duke body model,³⁹ this resulted in an error for the relative B_1^+ maps of ~9% in the heart and ~3% in the prostate. Additionally, neglecting the proton density introduces another bias to the maps, which, however, is expected to be relatively small.¹⁷ Another assumption is that the GRE images are measured in the linear FA regime. With the reference voltage and FA used in this work, this might not entirely hold true for all transmit channels. Especially for transmit channel one, because of its close position to the heart, it is likely that the linear regime was exceeded partially. A method that deals with the issue of large dynamic ranges of the transmit fields¹¹ was introduced recently and could be applied in the future to address this problem. However, even with these errors present in the relative B_1^+ maps, we did see a good qualitative agreement

between simulations based on these maps and validation measurements.

Another limitation concerning the dynamic pulse design comes from the fact that the calculated absolute B_1^+ maps were only estimations, relying on the scaling factor calculated from a single subject. Since the dynamic pulses were designed with a relatively low FA and the CoV does not change by multiplication with a constant factor, the results shown in this work should not be affected by this limitation. However, the actual FAs of the designed pulses would likely differ within a certain range around the target FA.³¹ To solve this problem, the dynamic pulses could be scaled by a subject-specific power calibration factor, which would require additional measurement time and would also scale the SED of the pulses quadratically. However, since both UP35-4kT and the tailored-4kT pulses would have to be scaled by the same factor for a specific subject, the SED reduction of the tailored-4kT pulses compared to UP35-4kT should remain unchanged. In the future and especially for the design of pTx pulses with larger FAs, the transferability of scaling factors should be investigated. Additionally, the development of fast and robust absolute B_1^+ mapping methods applicable for UHF body imaging is an ongoing research topic and might provide solutions for a rapid acquisition of absolute B_1^+ information.^{40,41}

More sophisticated reconstructions could be applied to further increase the acceleration and reduce the influence of undersampling⁴² and are currently being investigated for the use in B_1^+ mapping.⁴³ The main problem with more complex methods is the prolonged reconstruction time, which currently hinders their use in an online pulse design pipeline. Other promising approaches for reducing calibration times include deep learning methods, which might be able to shorten⁴⁴ or even completely remove⁴⁵ the time needed for B_1^+ mapping.

With the results shown in this work, an online calculation of tailored pTx pulses for heart and prostate in the range of a minute appears to be feasible. However, besides B_1^+ mapping, an online pulse design pipeline also includes reconstruction, segmentation and pulse optimization. Although the reconstruction of the data was done offline in this work, an online reconstruction for the DA-3D-rad sequence has already been implemented. Since gridding of the data can be done simultaneously to the measurement, the reconstructed images are available within a short time span.⁴⁶ The optimization of a tailored prostate phase shim was done in less than 5 s. The tailored-4kT pulses in the heart were calculated in ~10 s by using UP35-4kT as warm start.³² For the remaining challenge of an automated masking, deep learning approaches could be useful.

5 | CONCLUSION

In this work, the performance of universal pTx pulses for prostate and heart imaging at 7 T, as well as the feasibility of accelerating tailored pTx pulse design by using under-sampled B_1^+ maps were investigated. For the prostate a universal phase shim and for the heart a universal 4kT-point pulse yielded satisfying results but could still be improved by using tailored pulses, which were optimized on accelerated B_1^+ maps with an acquisition time of 30 s.

CONFLICT OF INTEREST STATEMENT

J.H., C.M., and R.K. are employees of Siemens Healthcare. T.L. is an employee of Rapid Biomedical. A.N. receives research support from Siemens Healthcare.

ACKNOWLEDGEMENT

Open Access funding enabled and organized by Projekt DEAL.

ORCID

Nico Egger  <https://orcid.org/0000-0002-7092-1847>

Laurent Ruck  <https://orcid.org/0000-0002-5978-3383>

Jürgen Herrler  <https://orcid.org/0000-0002-4620-8216>

Sebastian Schmitter  <https://orcid.org/0000-0003-4410-6790>

Armin Michael Nagel  <https://orcid.org/0000-0003-0948-1421>

REFERENCES

- Pohmann R, Speck O, Scheffler K. Signal-to-noise ratio and MR tissue parameters in human brain imaging at 3, 7, and 9.4 tesla using current receive coil arrays. *Magn Reson Med*. 2016;75:801-809.
- Le Ster C, Grant A, Van de Moortele PF, et al. Magnetic field strength dependent SNR gain at the center of a spherical phantom and up to 11. 7T. *Magn Reson Med*. 2022;88:2131-2138.
- Nagel AM, Schmitter S, Bock M, et al. Parameter optimization for 7T ^{23}Na -MRI. In *Proceedings of the 17th Annual Meeting of ISMRM*. Honolulu; 2009:2465.
- Gati JS, Menon RS, Ugurbil K, Rutt BK. Experimental determination of the BOLD field strength dependence in vessels and tissue. *Magn Reson Med*. 1997;38:296-302.
- Ladd ME, Bachert P, Meyerspeer M, et al. Pros and cons of ultra-high-field MRI/MRS for human application. *Prog Nucl Magn Reson Spectrosc*. 2018;109:1-50.
- Ibrahim TS, Lee R, Abduljalil AM, Baertlein BA, Robitaille P-ML. Dielectric resonances and B_1 field inhomogeneity in UHFMRI: computational analysis and experimental findings. *Magn Reson Imaging*. 2001;19:219-226.
- Ibrahim TS, Lee R, Baertlein BA, Kangarlou A, Robitaille P-ML. Application of finite difference time domain method for the design of birdcage RF head coils using multi-port excitations. *Magn Reson Imaging*. 2000;18:733-742.
- Hoult DI. Sensitivity and power deposition in a high-field imaging experiment. *J Magn Reson*. 2000;12:46-67.
- Webb AG, Collins CM. Parallel transmit and receive Technology in High-Field Magnetic Resonance Neuroimaging. *Int J Imag Syst Tech*. 2010;20:2-13.
- Pohmann R, Scheffler K. A theoretical and experimental comparison of different techniques for $B(1)$ mapping at very high fields. *NMR Biomed*. 2013;26:265-275.
- Padormo F, Hess AT, Aljabar P, et al. Large dynamic range relative B_1+ mapping. *Magn Reson Med*. 2016;76:490-499.
- de Buck MH, Kent JL, Jezzard P, Hess AT. Head-and-neck multichannel B_1+ mapping and RF shimming of the carotid arteries using a 7T parallel-transmit head coil. *Magn Reson Med*. 2024;91:190-204.
- Tenbergen CJA, Metzger GJ, Scheenen TWJ. Ultra-high-field MR in prostate cancer: feasibility and potential. *Magn Reson Mater Phys Biol Med*. 2022;35:631-644.
- Gras V, Vignaud A, Amadon A, Le Bihan D, Boulant N. Universal pulses: a new concept for calibration-free parallel transmission. *Magn Reson Med*. 2017;77:635-643.
- Aigner CS, Dietrich S, Schaeffter T, Schmitter S. Calibration-free pTx of the human heart at 7T via 3D universal pulses. *Magn Reson Med*. 2022;87:70-84.
- Van de Moortele P-F, Ugurbil K. Very fast multi channel B_1 calibration at high field in the small flip angle regime. In *Proceedings of the 17th Annual Meeting of ISMRM*. Honolulu; 2009:367.
- Dietrich S, Aigner CS, Kolbitsch C, et al. 3D free-breathing multichannel absolute B_1+ mapping in the human body at 7T. *Magn Reson Med*. 2021;85:2552-2567.
- Nagel AM, Laun FB, Weber MA, Matthies C, Semmler W, Schad LR. Sodium MRI using a density-adapted 3D radial acquisition technique. *Magn Reson Med*. 2009;62:1565-1573.
- Rink K, Benkhedah N, Berger MC, et al. Iterative reconstruction of radially-sampled $(31)\text{P}$ bSSFP data using prior information from $(1)\text{H}$ MRI. *Magn Reson Imaging*. 2017;37:147-158.
- Winkelmann S, Schaeffter T, Koehler T, Eggers H, Doessel O. An optimal radial profile order based on the Golden ratio for time-resolved MRI. *IEEE Trans Med Imaging*. 2006;26:68-76.
- Yarnykh VL. Actual flip-angle imaging in the pulsed steady state: a method for rapid three-dimensional mapping of the transmitted radiofrequency field. *Magn Reson Med*. 2007;57:192-200.
- Maggioni MB, Krämer M, Reichenbach JR. Optimized gradient spoiling of UTE VFA-AFI sequences for robust T_1 estimation with B_1 -field correction. *Magn Reson Imaging*. 2021;82:1-8.
- Petzold J, Ittermann B, Seifert F. Robustness of pTx safety concepts to varying subjects and subject positions. *Proceedings of the 29th Annual Meeting of ISMRM*, 2021 Abstract 2488.
- Uecker M, Ong F, Tamir JJ, et al. Berkeley advanced reconstruction toolbox. *Proceedings of the 23rd Annual Meeting of ISMRM*, Toronto, CA, 2015 Abstract 2486.
- Schmitter S, Wu X, Adriany G, Auerbach EJ, Ugurbil K, van de Moortele PF. Cerebral TOF angiography at 7T: impact of B_1+ shimming with a 16-channel transceiver array. *Magn Reson Med*. 2014;71:966-977.
- Berrington A, Povazan M, Mirfin C, et al. Calibration-free regional RF shims for MRS. *Magn Reson Med*. 2021;86:611-624.
- Cloos M, Boulant N, Luong M, et al. kT-points: short three-dimensional tailored RF pulses for flip-angle homogenization over an extended volume. *Magn Reson Med*. 2012;67:72-80.

28. Williams SN, McElhinney P, Gunamony S. Ultra-high field MRI: parallel-transmit arrays and RF pulse design. *Phys Med Biol*. 2022;68(2).
29. Majewski K, Ritter D. First and second order derivatives for optimizing parallel RF excitation waveforms. *J Magn Reson*. 2015;258:65-80.
30. Majewski K. Simultaneous optimization of radio frequency and gradient waveforms with exact Hessians and slew rate constraints applied to kT-points excitation. *J Magn Reson*. 2021;326:106941.
31. Aigner CS, Dietrich S, Schmitter S. Three-dimensional static and dynamic parallel transmission of the human heart at 7 T. *NMR Biomed*. 2021;34:e4450.
32. Herrler J, Liebig P, Gumbrecht R, et al. Fast online-customized (FOCUS) parallel transmission pulses: a combination of universal pulses and individual optimization. *Magn Reson Med*. 2021;85:3140-3153.
33. Boada FE, Christensen JD, Gillen JS, Thulborn KR. Three-dimensional projection imaging with half the number of projections. *Magn Reson Med*. 1997;37:470-477.
34. Fautz H, Vogel M, Gross P, Kerr A, Zhu Y. B1 mapping of coil arrays for parallel transmission. *Proceedings of the 16th Annual Meeting of ISMRM*, Toronto, CA, 2008 Abstract 1247.
35. Metzger GJ, Snyder C, Akgun C, Vaughan T, Ugurbil K, van de Moortele PF. Local B1+ shimming for prostate imaging with transceiver arrays at 7T based on subject-dependent transmit phase measurements. *Magn Reson Med*. 2008;59:396-409.
36. Mao W, Smith MB, Collins CM. Exploring the limits of RF shimming for high-field MRI of the human head. *Magn Reson Med*. 2006;56:918-922.
37. Wu X, Schmitter S, Auerbach EJ, Ugurbil K, Van de Moortele P-F. Mitigating transmit B1 inhomogeneity in the liver at 7T using multi-spoke parallel transmit RF pulse design. *Quant Imaging Med Surg*. 2014;4:4.
38. Runderkamp B, Roos T, van der Zwaag W, et al. B1+ homogenization in 3D liver MRI at 7 tesla using eight-channel parallel transmission: Kt-points vs. phase shimming. *Proceedings of the 29th Annual Meeting of ISMRM*, 2021 Abstract 3338.
39. Gosselin M-C, Neufeld E, Moser H, et al. Development of a new generation of high-resolution anatomical models for medical device evaluation: the virtual population 3.0. *Phys Med Biol*. 2014;59:5287-5303.
40. Lutz M, Aigner CS, Dietrich S, et al. Low Power Free-Breathing Absolute B1+ Mapping in the Human Body at 7T Using Magnetic Resonance Fingerprinting. *Proceedings of the 30th Annual Meeting of ISMRM*, London, UK, 2022 Abstract 0386.
41. Kent JL, Dragonu I, Valković L, Hess AT. Rapid 3D absolute B1+ mapping using a sandwiched train presaturated TurboFLASH sequence at 7 T for the brain and heart. *Magn Reson Med*. 2023;89:964-976.
42. Hess AT, Dragonu I, Chiew M. Accelerated calibration-less parallel transmit mapping using joint transmit and receive low-rank tensor completion. *Magn Reson Med*. 2021;86:2454-2467.
43. Kent JL, Valković L, Dragonu I, Chiew M, Hess AT. Accelerated volumetric Multi-Channel pTx B1+ mapping at 7T for the brain and heart. *Proceedings of the 31st Annual Meeting of ISMRM*, Toronto, CA, 2023 Abstract 4408.
44. Eberhardt B, Poser BA, Shah NJ, Felder J. B1 field map synthesis with generative deep learning used in the design of

parallel-transmit RF pulses for ultra-high field MRI. *Z Med Phys*. 2022;32:334-345.

45. Krueger F, Aigner CS, Hammernik K, et al. Rapid estimation of 2D relative B1+ maps from localizers in the human heart at 7T using deep learning. *Magn Reson Med*. 2023;89:1002-1015.
46. Müller M, Egger N, Sommer S, et al. Direct imaging of white matter ultrashort T2* components at 7 tesla. *Magn Reson Imaging*. 2021;86:107-117.

SUPPORTING INFORMATION

Additional supporting information may be found in the online version of the article at the publisher's website.

Figure S1. SoM of the receive fields B_1^- and transmit fields B_1^+ and correction factor $\Delta(\mathbf{r})$ needed to adjust for the assumption of equality between the two sum of magnitudes. The evaluation is shown for the electromagnetic field simulations of body model Duke for the heart (A) and prostate (B). The correction factor $\Delta(\mathbf{r})$ is calculated via:

$$\Delta(\mathbf{r}) = \sqrt{\frac{\sum_n^N |B_{1,n}^+(\mathbf{r})|}{\sum_m^N |B_{1,m}^-(\mathbf{r})|}}$$

and describes the factor that would need to be multiplied to the relative B_1^+ maps to correct for the assumption that the sum of magnitudes of the receive fields is equal to that of the transmit fields. As the simulations show, there are spatially dependent variations between the sum of magnitudes of receive and transmit fields. These variations lead to a mean correction factor for the heart of 0.92 ± 0.08 , which means that the relative B_1^+ maps will have a normalized error of $0.08/0.92 \approx 8.7\%$. For the prostate, the correction factor has a mean value of 0.97 ± 0.03 , resulting in a normalized error for the relative B_1^+ maps of $0.03/0.97 \approx 3.1\%$. Note that the factors were calculated for the 3D volumes of the heart/prostate of which only a 2D contour is shown.

Figure S2. Additional details of the RF coil array used in this work. (A) Dimensions of the upper and lower part of the transmit array and its individual loop elements. (B) Schematic of the arrangement of the individual receive loops (1–16) and combination of the loops in the transmit case (colors). (C) Exemplary setup of the RF coil for a phantom measurement.

Figure S3. (A) Selection of the value for σ for the Gaussian filter applied during the reconstruction of the accelerated B_1^+ maps. For an acceleration factor of 12, the B_1^+ maps were reconstructed with different values for σ and tailored-4kT pulses were calculated on these maps. The pulses were then evaluated on the original B_1^+ maps and the σ with the lowest median CoV ($\sigma = 3$ mm) was selected. (B) Point spread functions for the different reconstruction steps of the relative B_1^+ maps. The effective resolution, defined as the full width at half maximum of the point spread function, is 1.59×4 mm ≈ 6.4 mm for the unfiltered radial data and increases to 1.97×4 mm ≈ 7.9 mm for the Hamming

filter and to $2.51 \times 4 \text{ mm} \approx 10.0 \text{ mm}$ for a combination of Hamming and Gaussian filter.

Figure S4. Plots of the CoVs and efficiencies for different values of the regularization parameter λ used in the optimization of tailored phase shims for the heart (A) and prostate (B) and examples of over-/under-regularized phase shims (C, D). For the selection of the regularization parameter, individual phase shims were calculated for each of the 35/23 subjects with different values for λ and the CoVs and efficiencies were calculated. From these, the λ with the qualitatively best trade-off between CoV and efficiency was selected and resulted in a value of 0.025 for the heart (A) and 0.3 for the prostate (B). An example of a less ideal regularization is shown for the heart (C), where a λ of 1 leads to a phase shim with slightly increased efficiency, although at the cost of a considerably increased CoV. For the prostate (D), an example with a λ of 0 results in a phase shim with slightly better homogeneity, but only about half the efficiency as the phase shim with a λ of 0.3.

Figure S5. Distance to the isocenter over the distance to the mean organ position for the 35 heart subjects (A) and 23 prostate subjects (B). For both organs a correlation between the distance to the isocenter and the distance to the mean heart/prostate position is observable. This correlation is likely an explanation as to why the homogeneities and efficiencies also decrease for the tailored phase shims with increasing distance to the mean organ position as seen in Figure 3.

Figure S6. SoM images and channel-wise overview of the relative B_1^+ magnitude and phase maps of one heart subject (A) and one prostate subject (B) obtained for ACF 1, 10 and 20. The contours of the 2D masks corresponding to the illustrated slices are outlined in red. The lower SNR and noise-like undersampling artifacts resulting from the reduced number of measured projections are visible in the accelerated B_1^+ maps and increase with higher ACFs. Nevertheless, the general pattern of the B_1^+ magnitude and phase is still preserved even for high ACFs. Note that the undersampling artifacts visible in the SoM images are amplified since they are summed up over the images of the eight transmit channels.

Figure S7. (A) Channel-wise magnitude of the complex difference between the original B_1^+ maps and B_1^+ maps with different accelerations (2,6,10,20) for one heart subject. For the calculation of the complex difference and the RMSE, the relative B_1^+ maps were normalized by the mean signal intensity of the corresponding sum of magnitudes. The RMSE between the original maps $B_{1_{org},n}^+$ and accelerated maps $B_{1_{acc},n}^+$ was determined as:

$$RMSE = \sqrt{\frac{1}{N \cdot N_{Tx}} \sum_n^{N_{Tx}} |B_{1_{org},n}^+ - B_{1_{acc},n}^+|^2_{ROI}}$$
 where N is the number of voxels within the ROI and N_{Tx} is the number of transmit

channels. In (A) the RMSE values for this subject are given at the top left for each acceleration factor. (B) Boxplot of the RMSE values for each subject, calculated for different acceleration factors. A clear increase of the RMSE values can be observed for increasing acceleration factors. (C) Correlation between the RMSE values of (B) and the CoV values resulting from the tailored-4kT pulses that were calculated on the B_1^+ maps with different acceleration factors (see Figure 7B). A strong correlation with a correlation factor of 0.88 can be observed between the two variables.

Figure S8. (A) Channel-wise magnitude of the complex difference between the original B_1^+ maps and B_1^+ maps with different accelerations (2,6,10,20) for one prostate subject. Analogous to the heart, for the calculation of the complex difference and the RMSE, the relative B_1^+ maps were normalized by the mean signal intensity of the corresponding sum of magnitudes and the RMSE was determined as explained in S7. (B) Boxplot of the RMSE values of the relative B_1^+ maps of each prostate subject, calculated for different acceleration factors. Similar to the heart, the RMSE values increase for larger acceleration factors. (C) Correlation between the RMSE values of (B) and the efficiencies resulting from the tailored phase shims that were calculated on the prostate B_1^+ maps with different acceleration factors (see Figure 5D). In contrast to the tailored-4kT pulses in the heart (Figure S7C), no strong correlation between these two variables can be observed. This is likely due to the fact that the reduction of the efficiencies for different acceleration factors was only minor and also smaller than the inter-subject variations.

Figure S9. CoVs of subject 6 for tailored-4kT pulses calculated with different USF and two different reconstruction methods. For reconstruction method 1 (Reco 1), the first N_{Proj}/USF projections were used, whereas for reconstruction method 2 (Reco 2), every 1:USF: N_{Proj} projection was selected. Since the projections are distributed homogeneously over the whole measurement time, for method 2 effects resulting from motion should be closer to the data reconstructed with all projections, which the pulses are tested on. As depicted, the strong outlier values that were observed for subject 6 with reconstruction method 1 are strongly reduced with method 2 and are closer to the median calculated over the remaining 34 subjects. This suggests that the outliers for subject 6 are caused by motion. However, since the golden angle acquisition is designed for reconstructing consecutive projections, reconstruction method 1 was used as the preferred method.

Figure S10. Comparison of the CoV values of tailored-4kT pulses optimized on B_1^+ maps with different nominal resolutions. The B_1^+ maps with nominal resolution of 4 mm were reconstructed with a Hamming and Gaussian

filter (see Methods section), resulting in an effective resolution of approximately 10 mm (see Figure S3). For the retrospective reconstruction of the B_1^+ maps with lower nominal resolution, the acquired projections were truncated at the k-space position corresponding to a resolution of 6.3 mm. Here, no additional filters were applied during reconstruction, which (due to the PSF of the radial readout) also results in an effective resolution of 10 mm. The data was then zero-filled to a resolution of 4 mm, to enable the application of the same masks for both resolutions. To fulfill the Nyquist criterion (see Reference 33), only 4000 projections are required for the reconstructions with a resolution of 6.3 mm, compared to the 10 000 projections for the reconstructions with 4 mm. Tailored-4kT pulses were optimized on the B_1^+ maps with both resolutions and 4000 (TA = 144 s) and 833 (TA = 30 s) projections and then evaluated on the B_1^+ maps with $\Delta x = 4$ mm and 10 000 projections as ground truth. For both acquisition times, tailored-4kT pulses optimized on the B_1^+ maps with 4 mm resolution show a lower median CoV and smaller variations than tailored-4kT pulses optimized on the B_1^+ maps with 6.3 mm resolution. Note that the lower readout duration, resulting from truncating the data for the reconstruction of the B_1^+ maps with a resolution of 6.3 mm in the post-processing, leads to a reduction of the SNR by a factor of 0.52 compared to an acquisition with the same readout duration as for 4 mm. Therefore, the acquisition of B_1^+ maps with a resolution of 6.3 mm but the same readout duration as for the B_1^+ maps with 4 mm might lead to a better performance.

Figure S11. Evaluation of the over exaggeration caused by testing the universal pulses on subjects included in the training data set. (A) CoV values of a universal 4kT-pulse optimized on 25 randomly chosen subjects (UP25-4kT) and tested on the 10 excluded subjects. As a comparison, the CoV values achieved with UP35-4kT for the same 10 subjects are shown. Evaluating UP25-4kT on the 10 excluded subjects results in a median CoV of 11.3%, whereas evaluating UP35-4kT on these subjects yields a slightly lower median CoV of 10.6%. (B) CoV values resulting for the 23 prostate subjects when evaluating UPS23 and 23 different phase shims optimized on only 22 subjects (each omitting a different subject) and tested on the one excluded subject (rUPS22). For the UPS23 a median CoV of 7.9% and for the rUPS22 a median CoV of 8.2% is obtained. (C) Efficiencies resulting for UPS23 and the rUPS22 when applied to all 23 prostate subjects. The UPS23 yields a median efficiency of 90.9% and the rUPS22 a median efficiency of 90.8%.

How to cite this article: Egger N, Nagelstraßer S, Wildenberg S, et al. Accelerated B_1^+ mapping and robust parallel transmit pulse design for heart and prostate imaging at 7 T. *Magn Reson Med*. 2024;92:1933-1951. doi: 10.1002/mrm.30185